ARTICLE IN PRESS

Polymer xxx (xxxx) xxx



Contents lists available at ScienceDirect

Polymer

journal homepage: http://www.elsevier.com/locate/polymer



Nanocarrier-loaded block copolymer dual domain organogels

Kenneth P. Mineart^{a,*}, William W. Walker^a, Joaquin Mogollon-Santiana^a, Ian A. Coates^a, Cameron Hong^a, Byeongdu Lee^b

- ^a Department of Chemical Engineering, Bucknell University, Lewisburg, PA, 17837, USA
- ^b X-Ray Science Division, Argonne National Laboratory, Lemont, IL, 60439, USA

ARTICLE INFO

Keywords: Organogels Block copolymers Self-assembly

ABSTRACT

Loaded polymer gels are prevalent materials in the controlled release community and, fairly recently, have been formulated to include nanocarrier domains such as micelles and vesicles. One mechanism used to establish the solid-like characteristic of gels is block copolymer self-assembly, which can result in a system-spanning, physically-crosslinked network. The combination of nanocarrier and crosslink domain presence offers gels with a rich nanoscale phase space capable of intricate macroscopic property tuning. The current manuscript provides an overview of nanocarrier-loaded block copolymer organogels wherein nanocarriers are reverse micelles formed by sodium dioctyl sulfosuccinate (AOT), the block copolymer is a styrenic ABA triblock copolymer, and the gel solvent is aliphatic mineral oil. This introductory overview starts by identifying the envelope in ternary phase space wherein nanocarrier-loaded block copolymer organogels form (2–49 wt% triblock copolymer and 8x10⁻³-1 wt% AOT). Next, a detailed nanostructural description of gels varying in AOT and triblock copolymer concentration is presented. The manuscript concludes with demonstration of AOT reverse micelle release and gel uniaxial tensile response for gels containing 0–1 wt% AOT and 5–40 wt% styrenic triblock copolymer.

1. Introduction

Polymeric gels containing payload compounds - commonly referred to as loaded gels - have been of focus in the macromolecular and controlled release communities for a number of decades [1,2]. Major applications of loaded polymer gels include drug [2] and agricultural [3] delivery wherein payload compounds comprise pharmaceutical, therapeutic, fertilizer, or insecticide compounds. Within drug delivery, loaded gels have been applied as transdermal [4,5] and injectable [6,7] media, as well as, used for a range of treatments from ocular [8] to intestinal [9]. Arguably, the largest benefit of loaded polymer gels over their solution-based alternatives is the spatiotemporal control they enable. The solid-like characteristics of gels confines them to the site where they are applied whereas liquids are free to flow including to ineffective, or undesired, locations. Additionally, gels' macromolecules serve as barriers to diffusion, and their functionality and concentration can be used to tailor the rate of payload release [10,11]. The delivery rate from solution, on the other hand, is typically fixed based upon process variables. Two primary considerations in formulating loaded gels are the state of the payload compound and the mechanism of gel crosslinking.

Gel payload can exist either as freely dispersed molecules or as an encapsulant inside of nanocarrier domains. The former case leads to more straightforward formulation since less components are required, but dispersed payload is typically released rapidly and is liable to undergo significant 'burst' release wherein an undesirable discharge of payload occurs in the early stage of application [12]. Furthermore, the list of candidate payload compounds is restricted to those soluble in the gel solvent (e.g., payload dispersed in hydrogels must be relatively water-soluble). Recent work has shown that gels can alternatively be imbibed with micelles [13,14], or vesicles [15,16], that are capable of containing the payload compound. These approaches have shown considerably extended release times and reduction in 'burst' release [17, 18], and their unique internal environment (compared to the gel solvent) enables even solvent-insoluble payload compounds to be incorporated. Vesicles in particular offer outstanding flexibility in terms of potential payload candidates since they contain both hydrophilic and hydrophobic regions for encapsulation [19].

Gel crosslinking, on the other hand, is responsible for gels' solid-like behavior. Potential crosslinking methods grow more diverse with our expanding knowledge of polymer synthesis, but can generally be categorized as chemical or physical [20]. Chemical crosslinking involves

E-mail address: kpm007@bucknell.edu (K.P. Mineart).

https://doi.org/10.1016/j.polymer.2020.123246

Received 29 September 2020; Received in revised form 6 November 2020; Accepted 12 November 2020 Available online 21 November 2020 0032-3861/© 2020 Published by Elsevier Ltd.

^{*} Corresponding author.

covalent bonds that connect two or more polymer chains resulting in a system-spanning network. Alternatively, physical crosslinking joins multiple polymer chains through non-covalent interactions (e.g., hydrogen bonding, columbic attraction, crystallization, or phase immiscibility). The latter mechanism is beneficial in that non-covalent interactions are reversible providing gels with thermal-, solvent-, and/or shear-based sol-gel transitions, which enable gels to be processed, recycled, or injected post-crosslinking [4,21,22]. In contrast to covalent crosslinks, which exist at a length scale commensurate with small molecules (~0.1–1 nm), physical crosslinks are often much larger (~10 nm) due to the microphase separation processes they rely upon. Crosslinking via block polyelectrolyte self-assembly, for example, results in crosslinks as large as 10.5 nm and ranging in geometry from spheres to cylinders to lamellae [23].

Gels comprised of nanocarriers and large physical crosslinks offer a relatively complex nanoscale topology with a number of formulation knobs for tuning structure and consequently macroscopic properties. This manuscript's goal is to introduce a new class of gels, which we refer to as dual domain organogels (DDOGs), that are formed through physical crosslinking, contain nanocarrier domains, and are prepared with nonvolatile mineral oil as the solvent. More specifically, gels are prepared using the previously studied pairing of styrenic triblock copolymer and midblock-selective, aliphatic oil [24,25] combined with an amphiphile capable of forming reverse micelles (Fig. 1). These DDOGs offer several practical benefits over hydrogel analogues including the ability to be thermally processed well over 100 °C and a reduced dependence on environmental conditions (e.g., they do not dry out at low humidity).

2. Experimental details

2.1. Materials and sample preparation

The materials used in this study include sodium dioctyl sulfosuccinate (AOT, Scheme 1) (Sigma Aldrich, \geq 97%), 7,7,8,8-tetracyanoquinodimethane (TCNQ) (VWR International, \geq 98%), toluene (VWR

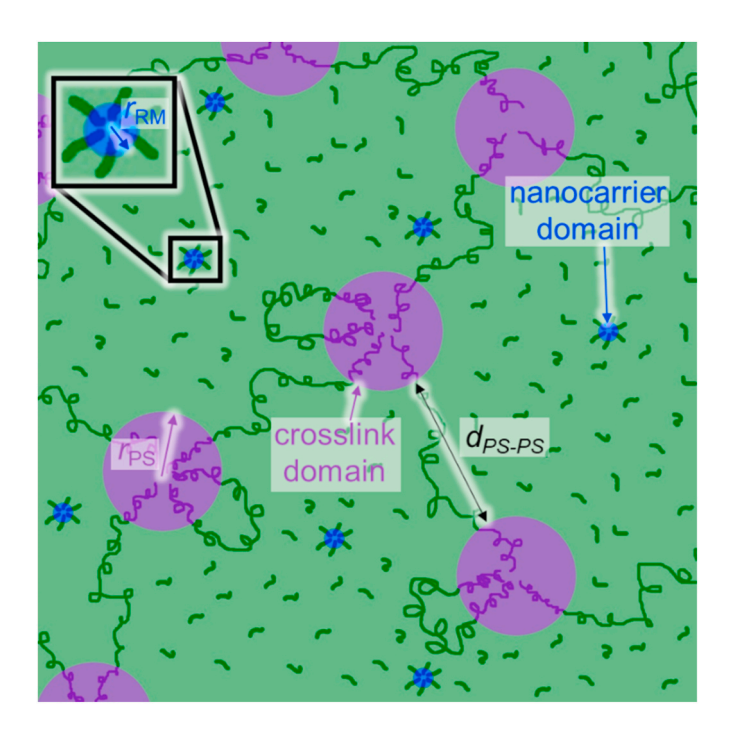


Fig. 1. A schematic representing the nanoscale structure within DDOGs. The two domain types and relevant geometric parameters are identified ($r_{\rm RM}=$ reverse micelle radius, $r_{\rm PS}=$ polystyrene crosslink radius, and $d_{PS-PS}=$ distance between polystyrene crosslinks).

International, reagent grade), poly[styrene-b-(ethylene-butylene)-b-styrene] (SEBS, Scheme 1) (Kraton Polymers LLC, grade G1654H, $M_{\rm n}=125~{\rm kDa},\, D=1.01, f_{PS}=0.33~{\rm g~PS/g})$, and white aliphatic mineral oil (MO) (Sonneborn LLC, grade Hydrobrite 200 PO). Of these, Kraton Polymers LLC and Sonneborn LLC generously provided SEBS and MO, respectively, and all compounds were used as received.

Solutions for small angle x-ray scattering (SAXS) experiments were prepared by directly dissolving AOT in MO at the desired concentration by mixing on a stir plate at 40 °C. Gels were prepared by dissolving SEBS, MO, and/or AOT each at its desired quantity in toluene at a 20:1 toluene volume to gel solids mass ratio (e.g., 2.0 g SEBS, 0.1 g AOT, and 7.9 g MO were dissolved in 200 mL toluene). Once complete dissolution was achieved as ascertained by eye, homogenous gels were extracted from toluene solutions by rotary evaporation (28.5 mmHg and 40 °C). Isolated gels were then annealed in a vacuum oven at $\approx\!35$ mmHg and 120 °C for approximately 18 h. Gels were subsequently formed into desired sample geometries using a Carver Press operated at 100–150 °C (depending on SEBS concentration) and minimal applied pressure.

2.2. CMC determination

To determine critical micelle concentration, cmc, solutions containing AOT, TCNQ, and MO are required. TCNQ was first dissolved in toluene at 3.5×10^{-2} wt%. Next, TCNQ-MO and TCNQ-AOT-MO master solutions were formulated by adding 1.0 g of the 3.5×10^{-2} wt% TCNQ-toluene solution per 15.0 g of MO, or 15.0 g of 1 wt% AOT in MO, solution. Toluene was removed from the resulting mixtures through rotary evaporation (28.5 mmHg and $40~^{\circ}$ C) for 3 h. Finally, a concentration series was created through 2^{n} serial dilution of the master TCNQ-AOT-MO solution using the TCNQ-MO solution. Solutions containing TCNQ were stored in dark conditions whenever possible to avoid light-induced degradation and UV-vis spectra were collected on a Hach DR6000 spectrophotometer.

2.3. SAXS experiments

Small angle x-ray scattering (SAXS) experiments were conducted on beamline 12-ID-B at the Advanced Photon Source (Argonne National Laboratory). Experiments used 13.3 keV x-ray radiation ($\lambda=0.93\,\text{Å}$) and a Pilatus 2M detector located at sample-to-detector distance, $l_{\rm sd}=2.01$ m. Experiments were performed at ambient temperature and pressure, and all samples were measured in transmission mode. Solutions were assessed using a 1.0-mm capillary flow-through cell to eliminate noise from capillary-to-capillary variation.

Raw two-dimensional SAXS intensity maps were converted into one-dimensional intensity profiles via azimuthal integration where the one-dimensional scattering vector, q, is related to the scattering half-angle, θ , and x-ray wavelength, λ , by $q=4\pi \sin(\theta)/\lambda$. Solution data was background corrected by subtraction of MO-filled capillary data. Alternatively, the MO contribution in gel data was removed by subtracting capillary-corrected MO data (i.e., MO in capillary data minus empty capillary data). All data was converted to absolute scale using glassy carbon as a reference. [26] One-dimensional profiles were fit using the SasView package (http://www.sasview.org/).

2.4. Release experiments

Gels were formed into disks with a diameter and thickness of 25 mm and 1.5 mm, respectively. Gel disks were placed into glass jars containing MO at a 3:100 gel mass to liquid MO volume ratio (e.g., 3.00 g gel submersed in 100 mL of MO). Jars were maintained at ambient temperature and were periodically agitated. To limit MO consumption and waste, the MO in jars was not replaced over the course of diffusion experiments. This factor is accounted for wherever necessary in the theoretical framework used to model resultant retained mass profiles. A comprehensive mathematical treatment can be found in our previous

Scheme 1. Chemical structures for SEBS and AOT. To correlate with Fig. 1, the polystyrene endblocks of SEBS are shown in purple, the ethylene-butylene midblock of SEBS and aliphatic AOT tails are shown in green, and the polar AOT headgroup is shown in blue.

publication [27]. Gravimetric and Fourier transform infrared spectroscopy (FTIR) measurements of gels were collected at regular intervals to track the amount of AOT retained in gels. MO present on gels' surface was wiped off prior to each measurement. FTIR data was collected using a Thermo Scientific Nicolet iS10 spectrometer maintained at ambient temperature and purged with N_2 . A spectral resolution of $0.5~\rm cm^{-1}$ was used and each spectrum is an average of 32 scans. No IR-transparent windows were required for analysis due to the freestanding nature of gels. Release data was fit using the fittype function in MATLAB.

2.5. Uniaxial tensile experiments

Uniaxial tensile testing of DDOG samples was performed on an ADMET eXpert 8000 planar biaxial tester (utilizing only one axis). Initial gel dimensions were ca. 7.6 mm (W) x 1.6 mm (T) and each formulation was tested in triplicate at a stretch rate of 0.01 sec $^{-1}$.

3. Results & discussion

3.1. Phase behavior

The first step in our exploration of DDOGs is theoretical consideration of their phase behavior. We start by exploring the (in)compatibility between the relevant groups present (*i.e.*, polystyrene (PS), poly [ethylene-butylene] (EB), MO, aliphatic AOT tails (AOT-t), and polar AOT headgroups (AOT-h)). An established method for predicting chemical compatibility is comparison of solubility parameters. Hansen solubility parameters, specifically, take into consideration the dispersive, polar, and hydrogen-bonding interactions that contribute to the compatibility of various compounds [28,29]. The ultimate characteristic of compatibility from the Hansen solubility parameter approach is solubility distance, R_{a} , for which lower values reflect compounds that are more compatible. In this approach, solubility distance is computed by

$$R_{a} = \sqrt{4(\delta_{d1} - \delta_{d2})^{2} + (\delta_{p1} - \delta_{p2})^{2} + (\delta_{hb1} - \delta_{hb2})^{2}}$$
(1)

where δ_{di} , δ_{pi} , and δ_{hbi} are the dispersion, polar, and hydrogen-bond solubility parameters of component i and subscripts 1 and 2 are for the two components under consideration. Details regarding calculation of all solubility parameters are given in the Supporting Information (Tables S1-S5). The resultant value of R_a for a pair of compounds is then compared with the maximum allowable value for solubility to occur, R_0 , which is system dependent. Previous studies have shown that R_0 values for organic systems are $\approx 3.9-5$ MPa $^{1/2}$ [30–32]. Additionally, others' have demonstrated that SEBS/MO mixtures yield mostly pure PS and mixed EB/MO phases [25,33,34], which further confirms this R_0 range since R_a for PS/EB (immiscible) and EB/MO (miscible) are 4.9 and 3.9, respectively (Table 1). The full matrix of R_a values for pairs of interest (Table 1) suggests two things. First, PS and AOT-h should each phase

Table 1 Solubility distance, R_a , values (in MPa^{1/2}) for compound pairs of interest. Values less than ca. 4.0 suggest compatibility. Green, yellow, and red shading reflect the tendency of EB, MO, and AOT-t to mix, PS to microphase separate, and AOT-h to microphase separate, respectively.

| | PS | EB | МО | AOT-t | AOT-h |
|-------|------|------|------|-------|-------|
| PS | 0.0 | - | - | - | - |
| EB | 4.9 | 0.0 | - | - | - |
| МО | 8.6 | 3.9 | 0.0 | - | - |
| AOT-t | 7.0 | 2.2 | 1.7 | 0.0 | _ |
| AOT-h | 28.8 | 29.9 | 31.6 | 30.9 | 0.0 |

separate into their own, nearly pure phases. Second, EB, MO, and AOT-t should form a single well-mixed phase. These results, combined with the covalent connectivity of AOT-h and AOT-t, as well as, PS and EB, theoretically support the nanostructure presented in Fig. 1.

The phase behavior described by Hansen solubility parameter theory must be experimentally validated. The phase separation of PS endblocks in similar SEBS/MO gels has already been shown through a combination of electron microscopy and simulation [25,33]. To further confirm this fact, inverted vial tests were conducted to identify the SEBS gel point concentration, c_{gel} , with and without 1 wt% AOT. For the particular grade of SEBS employed in this study, c_{gel} was determined to be 2 wt% and is independent of the presence of 1 wt% AOT (Figure S1). Formation of gels at such a low copolymer concentration would not be possible in the absence of polystyrene phase separation.

Alternatively, AOT assembly into reverse micelles can be detected through characterization of the critical (reverse) micelle concentration, cmc, which is defined as the lowest concentration at which (reverse) micelles form. The cmc of AOT in MO was determined using the TCNQ probe method [35,36]. This method takes advantage of the unique ability of TCNQ molecules to convert from a neutral species in nonpolar environments (i.e., free AOT in solution) to a radical-anion species in polar/charged environments (i.e., when encapsulated in AOT reverse micelles). The molecular transformation is accompanied by emergence of visible light absorption at 750 nm and 850 nm (Fig. 2a). Furthermore, the magnitude of absorbance at each wavelength increases with encapsulated TCNQ concentration, which consequently increases with the number of reverse micelles present in solution. These factors lead to two distinct regions on an absorbance- w_{AOT} plot: (i) low w_{AOT} where

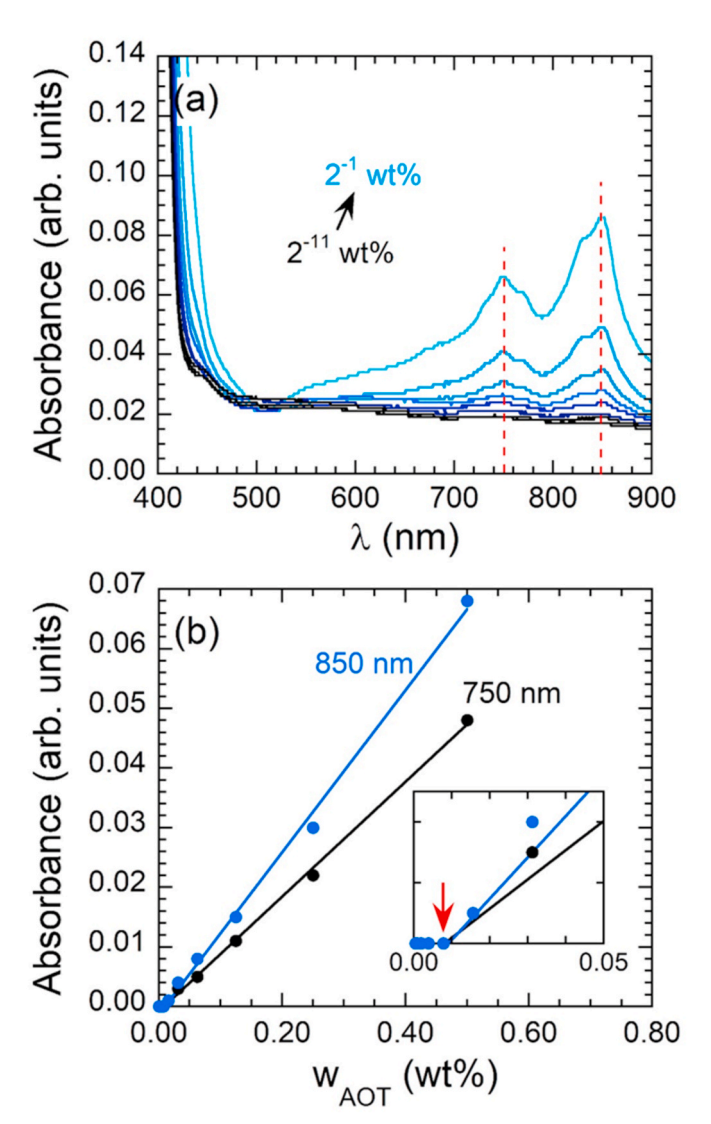


Fig. 2. UV–vis spectra from AOT-TCNQ-MO solutions (AOT concentration indicated, 3.5×10^{-2} wt% TCNQ) (a) and extracted peak absorbance values for 750 nm and 850 nm (b). The inset in (b) is a magnified view and the arrow indicates the *cmc* value.

absorbance is small and independent of w_{AOT} and (ii) high w_{AOT} where absorbance increases with w_{AOT} . The concentration at which a crossover from region (i) to region (ii) occurs defines the cmc (Fig. 2b). Our measurements indicate that AOT exhibits a cmc in MO confirming AOT self-assembly. Furthermore, the cmc value ($\approx 8x10^{-3}$ wt%) is in good agreement with others' work [37] on AOT in cyclohexane (a chemically-similar solvent).

Beyond validation of theoretically expected (in)compatibility, the SEBS gel point and AOT critical micelle concentration provide half of the information necessary to define the DDOG phase space on a ternary SEBS-AOT-MO phase diagram. The remaining two boundaries required to form an enclosed phase envelope are the maximum SEBS and AOT concentrations. We invoke the definition of a gel as a crosslinked material *primarily composed of liquid* in order to set the maximum SEBS concentration at 49 wt%. Alternatively, the maximum AOT concentration is defined by the saturation point of AOT in gels, c_{sat} . Above this amount, increasing AOT concentration only translates to an increasing presence of phase-separated AOT precipitate. From visual observation, SEBS-AOT-MO gels become translucent around 2 wt% AOT suggesting c_{sat} has been exceeded. Structural characterization of gels (via SAXS), as discussed below, supports this observation and further clarifies that AOT

forms precipitate phase just over 1 wt% AOT. The DDOG phase envelope is, therefore, defined by 2–49 wt% SEBS, $8x10^{-3}$ -1 wt% AOT, and balance MO (Fig. 3).

3.2. DDOG nanostructure

With the DDOG phase envelope defined, a systematic investigation of DDOG structure can now be conducted. Gels varying in AOT and SEBS concentrations (w_{AOT} and w_{SEBS} , respectively) were formulated (as shown by the points in Fig. 3) and characterized using SAXS. Prior to discussing these results, it is important to establish the SAXS model used to interpret scattering profiles:

$$I(q) = \varphi_{RM} \Delta \rho_{RM}^2 V_{RM} P_{RM}(q) + \varphi_{PS} \Delta \rho_{PS}^2 V_{PS} P_{PS}(q) S_{PS}(q) + bkg$$
(2)

The first portion of the model – with each term denoted by an RM subscript – reflects the contribution from reverse micelles, the second part – with each term denoted by a PS subscript – reflects the contribution from polystyrene crosslinks, and the final term – bkg – reflects incoherent background scattering. Additionally, φ_i , $\Delta \rho_i$, P_i (q), and S_i (q) are the volume fraction, scattering length density contrast (see Table S6 for values), q-dependent form factor, and q-dependent structure factor of i domains, respectively, and V_i is the volume of a single i domain. The form factors in this expression represent the shape of individual domains. Both reverse micelle and polystyrene domains are anticipated to be spherical, at concentrations of interest, based on current literature [34,38] and so take the form

$$P_i(q) = \left[\frac{\sin(qr_i) - qr_i\cos(qr_i)}{(qr_i)^3}\right]^2 \tag{3}$$

where r_i is the i domain radius. Additionally, a distribution of polystyrene domain size was taken into consideration through inclusion of a Schulz distribution of r_i with a dispersity of 0.08. As is implicit in Equation (2), S_i (q) is only relevant for polystyrene domains since they are of sufficient concentration for inter-domain structure to play a role. Reverse micelles are too dilute for inter-domain scattering (i.e., $S(q) \approx$

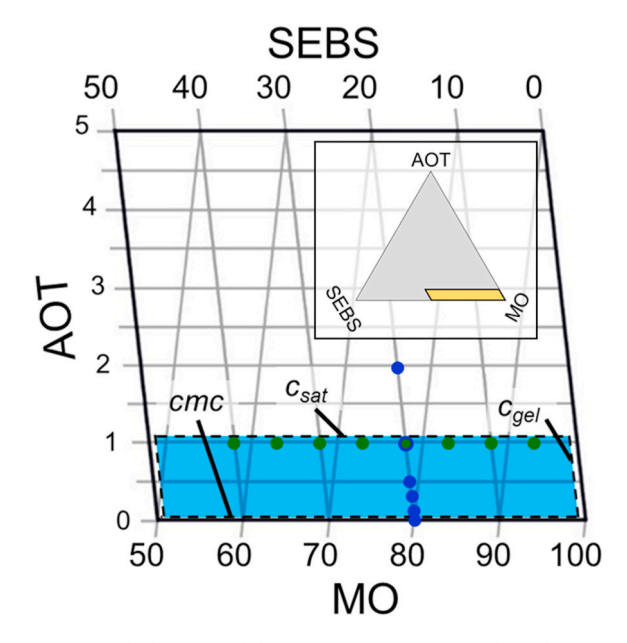


Fig. 3. A magnified section of the SEBS-AOT-MO ternary phase diagram with DDOG envelope indicated (dashed line, blue highlighting). Points show gel compositions structurally examined using SAXS, and the inset shows the ternary diagram in its entirety highlighting the region of magnification (yellow outlined region). Note, the magnified diagram is compressed horizontally for clarity. (For interpretation of the references to colour in this figure legend, the reader is referred to the Web version of this article.)

1). A hard sphere model is used to capture the liquid-like ordering of polystyrene domains

$$S_{PS}(q) = 1 + 4\pi \left(\frac{\varphi_{hs}}{4\pi r_{hs}^3/3}\right) \int_{0}^{\infty} (g(r) - 1) \left(\frac{\sin(qr)}{qr}\right) r^2 dr$$
 (4)

where r_{hs} is the polystyrene domain hard sphere radius (i.e., half the average center-to-center distance between domains), φ_{hs} is the volume fraction of these hard spheres, and g(r) is their radial distribution function [39]. The distance between polystyrene domains (d_{PS-PS}) is defined by $2(r_{hs} - r_{PS})$.

To begin our structural investigation, we first examine the effect of w_{AOT} and hence focus primarily on reverse micelle structure. Prior to probing reverse micelle structure within gels, we survey the simpler case of their presence in pure MO solutions. SAXS experiments conducted on AOT-MO solutions ranging in AOT concentration from 2^{-4} wt% (i.e., 6.25x10⁻² wt%) to 2¹ wt% reveal scattering profiles mostly consistent with dilute spheres (Fig. 4a). (An upturn at $q < 2x10^{-2} \text{ Å}^{-1}$ indicates that a small fraction of AOT molecules may participate in the stabilization of micro-scale water droplets.) These profiles can be modeled using a simplified form of Equation (2) wherein only reverse micelles are accounted for (i.e., by eliminating the polystyrene domain term, $\varphi_{PS} =$ 0). Model fitting shows that AOT reverse micelles maintain a core radius of 9.5 \pm 0.1 Å regardless of AOT concentration. Moreover, the intensity of reverse micelle scattering (reflected by the plateau intensity at $q \approx$ $3x10^{-2}$ - $6x10^{-2}$ Å⁻¹) increases with AOT concentration due to an increase in φ_{RM} . Fitted φ_{RM} values match closely with theoretical prediction ($\varphi_{RM} = w_{AOT}\rho_{soln}/\rho_{AOT}$ where ρ_{soln} and ρ_{AOT} are the densities of the solution and AOT, respectively) (Fig. 4c).

Next, gels formulated with the same concentrations of AOT and a fixed w_{SEBS} of 20 wt% (blue points in Fig. 3) were examined. Alongside scattering from SEBS self-assembly ($q \le 10^{-1} \text{ Å}^{-1}$), the gel SAXS profiles contain similar reverse micelle scattering behavior ($q \approx 10^{-1} \cdot 10^{0} \text{ Å}^{-1}$) as that noted in solutions (Fig. 4b) and are well described by the full form of Equation (2). (An upturn is, once again, evident at $q < 10^{-2} \,\text{Å}^{-1}$, but in this case likely arises from larger copolymer aggregates since it is also observed in gel SAXS profiles in the absence of AOT, see Figure S2.) Model fits, again, indicate that AOT reverse micelles maintain a radius independent of w_{AOT} , but at a value lower than solutions (9.3 \pm 0.1 Å). The slightly smaller radius may reflect the fact that gels are annealed at elevated temperature and under vacuum, which could remove residual water from reverse micelles. Fitted φ_{RM} values from gels are similar to solution values, and for the most part are close to theoretical expectation (Fig. 4c). Finally, it is clear that varying w_{AOT} in gels does not alter the structural aspects of copolymer assembly. The r_{PS} (9.7 \pm 0.2 nm), d_{PS-PS} $(23.3 \pm 0.3 \text{ nm})$, and φ_{PS} $(5.8 \pm 0.1 \text{ vol}\%)$ values remain constant.

One feature in 20 wt% SEBS/1–2 wt% AOT gels that is not captured by model fitting is the presence of a sharp peak at $q \approx 3 \text{x} 10^{-1} \text{ Å}^{-1}$. This peak, which appears in a small fraction of the 1 wt% AOT gels (across the SEBS concentration range) and all 2 wt% AOT gels, is in close correspondence with the 10 diffraction peak of pure AOT's hexagonal columnar phase ($d_{10} = 2\pi/q \approx 20.9 \text{ Å}$) [40] suggesting the presence of AOT precipitate. Simultaneously, the φ_{RM} for gels containing 2 wt% AOT (Fig. 4c) is below expectation suggesting that not all AOT is participating in reverse micelle formation. As alluded previously, this evidence aided in assigning c_{sat} on the ternary phase diagram (Fig. 3).

The next logical step in investigating DDOG nanoscale structure is to examine the effect of varying w_{SEBS} . In contrast to the gel profiles discussed above, scattering from gels varying in SEBS concentration (with 1 wt% AOT, see green points in Fig. 3) undergo variations in the $q \le 10^{-1} \text{ Å}^{-1}$ region and remain relatively unchanged at $q \approx 10^{-1} \cdot 10^{0} \text{ Å}^{-1}$ (Fig. 5a). The diffuse peaks located at $q \approx 4 \times 10^{-2} \cdot 1 \times 10^{-1} \text{ Å}^{-1}$, which capture polystyrene domain size, shift to lower q values with increasing SEBS concentration. Additionally, the primary peak at $q \approx 1 \times 10^{-2} \cdot 10^{-2} \text{ Å}^{-1}$ (along with its secondary peak at $q \approx 3 \times 10^{-2} \text{ Å}^{-1}$), which

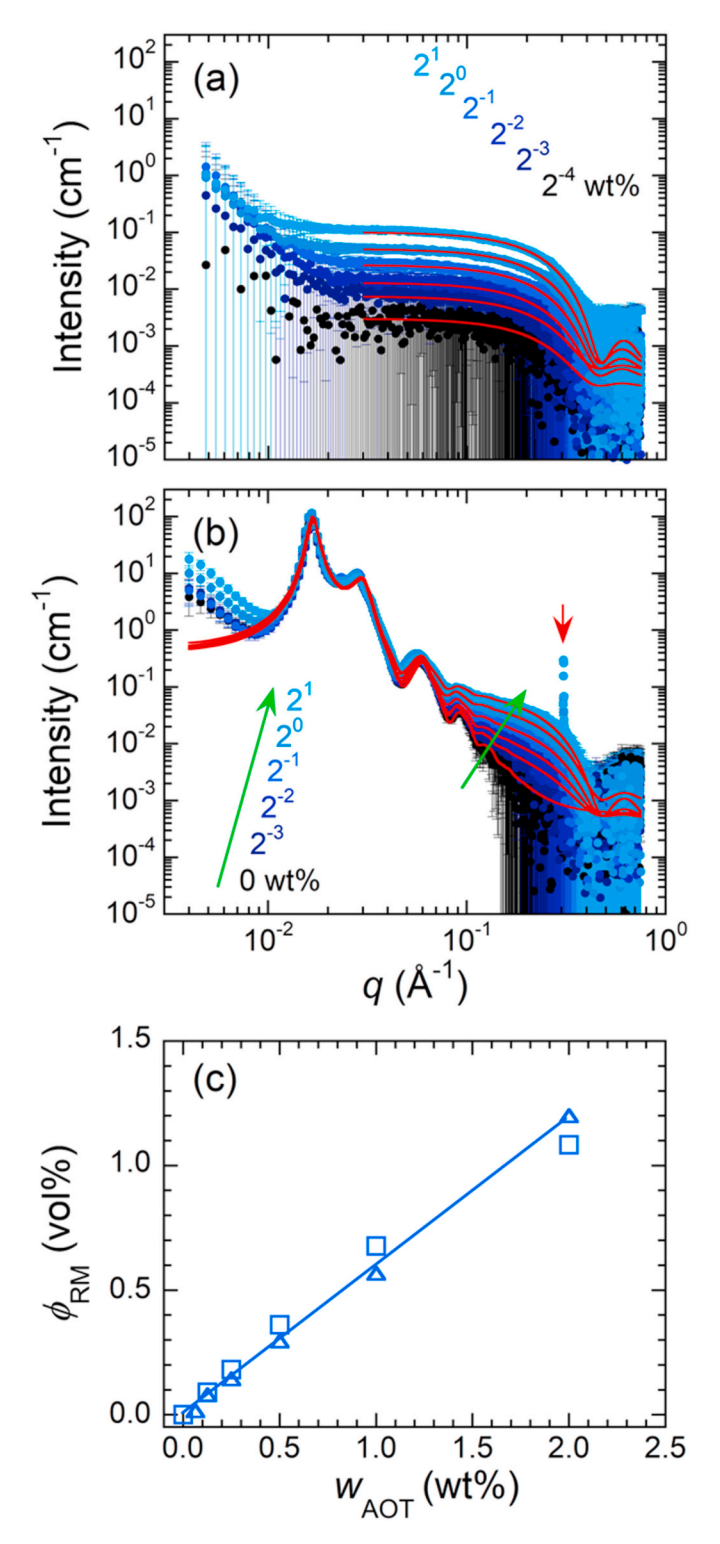


Fig. 4. 1D SAXS profiles for AOT-MO solutions (a) and SEBS-AOT-MO gels containing 20 wt% SEBS (b) (AOT concentrations indicated), as well as, fitted reverse micelle volume fractions from AOT-MO solutions (triangles) and SEBS-AOT-MO gels (squares) (c). Red solid lines in (a) and (b) indicate fitting using Equation (2). In (a), fitting was performed at $q>0.03~{\rm \AA}^{-1}$ and with $\varphi_{PS}=0$. In (b), the red arrow highlights a diffraction peak associated with AOT precipitate. The solid line in (c) shows the anticipated reverse micelle volume fraction based on formulated quantities. (For interpretation of the references to colour in this figure legend, the reader is referred to the Web version of this article.)

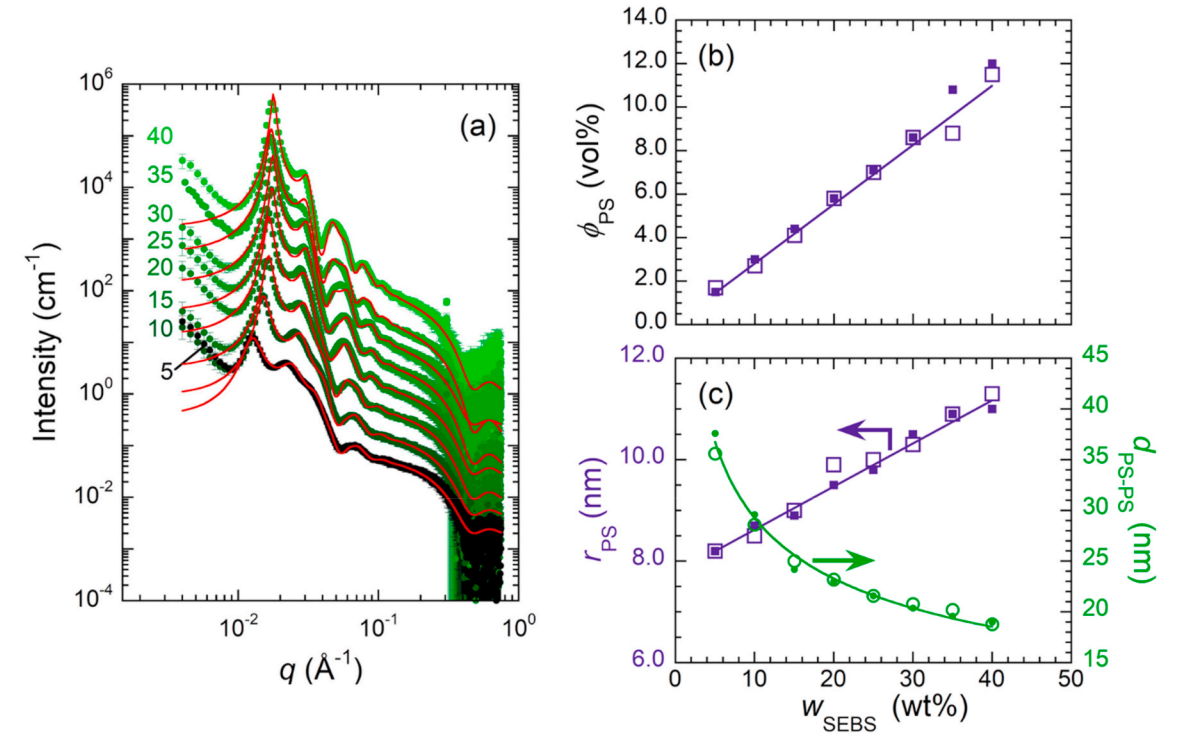


Fig. 5. 1D SAXS profiles for SEBS-AOT-MO gels containing 1 wt% AOT (a) (SEBS concentration indicated in units of wt%) and dependence of polystyrene domain volume fraction (b), polystyrene domain radius (c), and distance between polystyrene domains (c) on SEBS concentration. Data in (a) are shifted by a factor of 3^n for clarity (5 wt% SEBS is original scale) and red solid lines indicate fits using Equation (2). Open and closed symbols in (b) and (c) are for samples with 1 wt% and 0 wt% AOT, respectively, and solid lines reflect anticipated values based on formulated quantities (b), a linear fit (c, r_{PS}), and a guide to the eye (c, d_{PS-PS}). (For interpretation of the references to colour in this figure legend, the reader is referred to the Web version of this article.)

reflects polystyrene domain spacing, shifts to higher q values and becomes sharper with increasing SEBS concentration. As before, quantitative values of each structural feature can be determined by fitting profiles with Equation (2). The first observation from model fitting is that reverse micelles remain relatively unchanged in size ($r_{RM}=9.3\pm$ 0.1 Å) and concentration ($\varphi_{RM} = 0.6 \pm 0.1 \text{ vol}\%$). Second, φ_{PS} maintains good agreement with theoretical expectation (Fig. 5b) and polystyrene domain radius increases linearly from ca. 8.0 nm for $w_{SEBS} = 5$ wt% to ca. 11.0 nm for $w_{SEBS} = 40$ wt% (Fig. 5c). The increase in r_{PS} can be explained by a drive for decreased interfacial curvature as polystyrene concentration in gels (as represented by $f_{PS}w_{SEBS}$) increases. The distance between polystyrene domains, on the other hand, decreases monotonically with increasing w_{SEBS} (Fig. 5c) due to decreased swelling of the EB/MO matrix. Scattering profiles from gels containing 0 wt% AOT, and corresponding fitting, show that these nanostructural trends are unaffected by AOT presence (Figures S2 and 5b-c).

3.3. Macroscopic DDOG properties

For the final part of this manuscript, two macroscopic DDOG properties are presented, namely reverse micelle transport and gel mechanical behavior. Reverse micelle mobility can be experimentally measured using an FTIR-based protocol and corresponding theory that is described in our previous work [27]. In short, gels are submerged in pure MO imparting a reverse micelle concentration gradient that causes their passive diffusion from gels to the surrounding supernatant MO. The AOT ester groups (see Scheme 1) exhibit an isolated peak in gels' FTIR spectra at 1739 cm⁻¹ (Fig. 6a–b), which is used to track AOT concentration with time. Gel swelling during submersion is accounted for in this analysis using polystyrene groups' phenyl overtone peaks at 1940 cm⁻¹, 1870 cm⁻¹, and 1800 cm⁻¹ (Fig. 6a–b). Finally, control samples containing 0 wt% AOT are used for background correction. The data extracted from these experiments are in the form of retained AOT mass ($m_{AOT,t}/m_{AOT}$).

 $_{0}$ where $m_{AOT,t}$ and $m_{AOT,0}$ are the masses of AOT in gels at times t and 0, respectively) as a function of submersion time (Fig. 6c).

Retained AOT mass profiles were determined for DDOGs containing 5-40 wt% SEBS and 1 wt% AOT (initially) (Fig. 6c). As might be expected, increasing SEBS concentration leads to decreased mobility of reverse micelles. The time required for 95% release of AOT (i.e., 5% retained AOT), for example, increases dramatically from ≈200 h when $w_{SEBS} = 5$ wt% to ≈ 1200 h when $w_{SEBS} = 40$ wt%. Furthermore, profiles can be fitted using an empirical first-order release model defined by $m_{AOT,t}/m_{AOT,0} \propto e^{-kt}$ where k is the first-order rate constant and t is time. This model fits all gel data reasonably well (Fig. 6c), does not make any assumptions about sample geometry, and k quantitatively reflects the relative mobility of AOT reverse micelles with higher values indicating faster release. As qualitatively observed above, k values show a decrease of reverse micelle mobility with increasing SEBS concentration undergoing a reduction of \approx 85% from 5 wt% to 40 wt% SEBS (Fig. 6d). This large mobility decrease likely stems from a decrease in gel correlation length, also referred to as mesh size (ξ) , which affects hydrodynamic drag on reverse micelles and constricts their diffusion pathway, since scaling arguments show that $\xi \propto w_{EB(EB/MO)}^{-3/4} \propto w_{SEBS}^{-3/4}$ where $w_{EB(EB/MO)}$ is the concentration of EB within the EB/MO matrix [41]. Additionally, d_{PS-PS} may play a minor role in reducing reverse micelle mobility with increasing w_{SEBS} (see Fig. 5c), but is expected to be considerably less impactful compared with ξ due to their relative size scales $(d_{PS-PS}/\xi \approx$ 5–10, calculation and values of ξ can be found in the Supporting Information).

Diffusivity values can also, in theory, be extracted from the profiles shown in Fig. 6c using Fick's second law (see Supporting Information for details). The derived expression, however, assumes constant gel thickness and volume, which is not satisfied over the course of current release experiments (i.e., gels swell as much as 35% and 105% in terms of thickness and volume, respectively). That being said, the Fickian model describes retained mass profiles reasonably well (mathematically) when

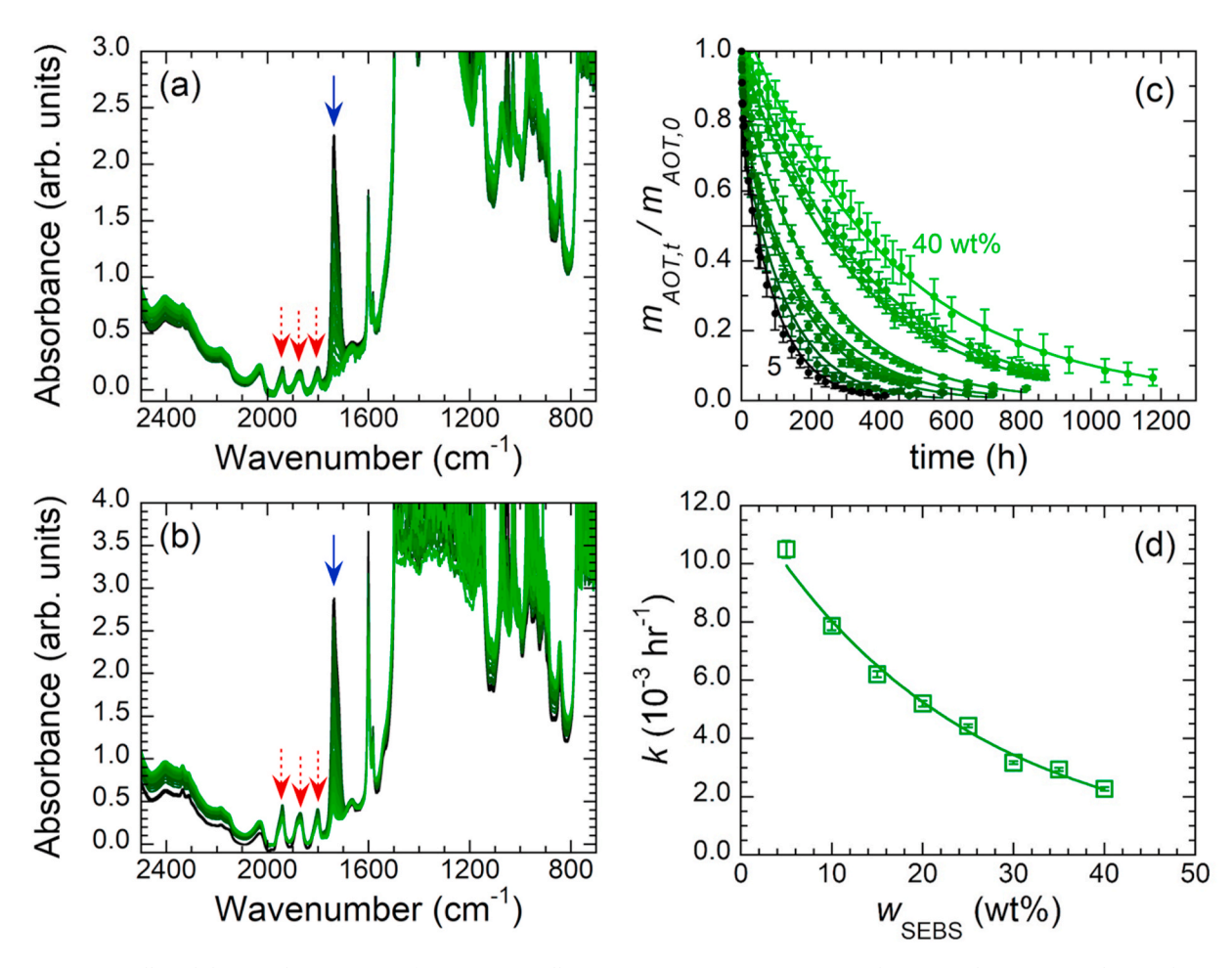


Fig. 6. FTIR spectra collected during submersion time for DDOGs initially containing 15 wt% (a) or 30 wt% (b) SEBS and 1 wt% AOT along with retained mass profiles for 1 wt% AOT gels varying in SEBS concentration (c) (increments of 5 wt%) and fitted first-order rate constants for AOT reverse micelle release from DDOGs (d). The blue solid and red dashed arrows in (a) and (b) indicate the positions of the AOT ester and PS phenyl peaks, respectively, and the solid lines in (c) and (d) are first-order release fits and a guide to the eye, respectively. (For interpretation of the references to colour in this figure legend, the reader is referred to the Web version of this article.)

 $w_{SEBS} \leq 20$ wt% (Figure S3) and allows diffusivity to be roughly approximated: $(5.3 \pm 1.5) \times 10^{-9}$ cm [2]/s for $w_{SEBS} = 20$ wt% to $(9.4 \pm 1.5) \times 10^{-9}$ 0.9)x 10^{-9} cm²/s for $w_{SEBS} = 5$ wt%. For comparison, diffusion of reverse micelles in MO can be calculated using the Stokes-Einstein equation (D_0 $= k_B T / 6\pi \mu r_{hy}$ where D is diffusivity, k_B is Boltzmann's constant, T is absolute temperature, μ is viscosity, and r_{hy} is the reverse micelle hydrodynamic radius). Previous studies find that r_{hy} of AOT reverse micelles in dodecane is $\approx 17~\text{Å}$ [42] and our viscometry measurements give $\mu=84.7$ mPa s (measured with Brookfield DVE Viscometer) resulting in $D_0 \approx 1.5 \text{x} 10^{-8} \text{ cm}^2/\text{s}$. The present analysis indicates that the relative diffusivity in gels compared to pure solvent (D/D_0) ranges between 0.35 and 0.62 further supporting the proposition that reverse micelles reside in the EB/MO matrix. If reverse micelles were instead to exist in polystyrene crosslink domains, their diffusion would be considerably slower due to the glassy state of polystyrene at room temperature. This is indirectly highlighted by others' measured diffusivity value for trace styrene monomer diffusing through polystyrene near ambient temperature ($D \sim 10^{-14} \text{ cm}^2/\text{s}$) [43,44].

Gels' mechanical behavior was characterized using quasistatic uniaxial tensile testing. These tests enable tensile stress, σ , to be determined at increasing values of axial stretch, λ_{zz} (= L/L_0 where L and L_0 are sample length and initial sample length, respectively). Stress-stretch data (Fig. 7) indicate a number of factors regarding DDOGs' mechanical properties. First, they show that gels are very tough materials that exhibit nonlinear elastic behavior and are capable of achieving large

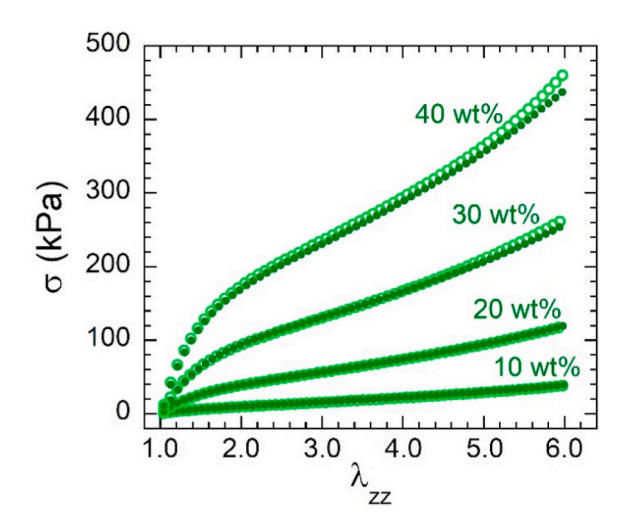


Fig. 7. Representative stress-stretch profiles for gels with varying w_{SEBS} (indicated). Data are from gels containing 0 wt% (open symbols) and 1 wt% (closed symbols) AOT.

deformation without breaking. Second, gels become less compliant (i.e., stiffer) as w_{SEBS} increases. Lastly, and most importantly, stress-stretch profiles suggest that the presence of reverse micelles ($w_{AOT}=1$ wt%)

do not have an appreciable effect on gels' tensile behavior. The former points agree with previous studies on SEBS/MO gels not containing AOT [22,45] while the latter highlights that the physically-crosslinked copolymer network is entirely responsible for gels' mechanical behavior.

4. Conclusion

This manuscript introduced DDOGs as physically-crosslinked, oilbased gels that contain nanocarriers. In our initial exploration of these materials, we presented the phase behavior, nanostructure, reverse micelle transport, and tensile response of SEBS/AOT/MO gels. DDOGs of this variety offer many benefits over other loaded gels (many of which are chemically crosslinked hydrogels) including an ability to be thermally processed and recycled, greater environment-independent stability, considerably extended release of loaded compound(s) (partially due to MO's high viscosity relative to water, $\mu_{MO} \approx 85 \mu_{H2O}$), and high elasticity and toughness. Furthermore, styrenic triblock copolymers and aliphatic mineral oils are commercially available enabling these materials to be produced on a large scale. We anticipate that judicious formulation design will allow detailed structure-property relationships to be developed for DDOGs in the near future and that these relationships will be broadly applicable to gels comprised of nanocarriers and physical crosslinks.

Declaration of competing interest

The authors declare that they have no known competing financial interests or personal relationships that could have appeared to influence the work reported in this paper.

Acknowledgments

We want to thank the NSF Division of Materials Research (award no. 1904047), the NSF Division of Civil, Mechanical and Manufacturing Innovation (award no. 1828082), and Bucknell University for financial support. We also want to thank Sonneborn, LLC for providing MO and Kraton Polymers, LLC for supplying SEBS. This work used resources at the Advanced Photon Source, a U.S. Department of Energy (DOE) Office of Science User Facility operated for the DOE Office of Science by Argonne National Laboratory under Contract No. DE-AC02-06CH11357.

Appendix A. Supplementary data

Supplementary data to this article can be found online at https://doi.org/10.1016/j.polymer.2020.123246.

References

- Y. Liang, L. Li, R.A. Scott, K.L. Klick, 50th anniversary perspective: polymeric biomaterials: diverse functions enabled by advances in macromolecular chemistry, Macromolecules 50 (2) (2017) 483–502, https://doi.org/10.1021/acs. macromol.6b02389.
- [2] M. Pitorre, H. Gondé, C. Haury, M. Messous, J. Poilane, D. Boudaud, E. Kanber, G. A. Rossemond Ndombina, J.-P. Benoit, G. Bastiat, Recent advances in nanocarrier-loaded gels: which drug delivery technologies against which diseases? J. Contr. Release 266 (2017) 140–155, https://doi.org/10.1016/j.jconrel.2017.09.031.
- [3] S.-B. Lao, Z.-X. Zhang, H.-H. Xu, G.-B. Jiang, Novel amphiphilic chitosan derivatives: synthesis, characterization and micellar solubilization of rotenone, Carbohydr. Polym. 82 (4) (2010) 1136–1142, https://doi.org/10.1016/j. carbpol.2010.06.044.
- [4] T.-M. Don, M.-L. Huang, A.-C. Chiu, K.-H. Kuo, W.-Y. Chiu, L.-H. Chiu, Preparation of thermo-responsive acrylic hydrogels useful for the application in transdermal drug delivery systems, Mater. Chem. Phys. 107 (2) (2008) 266–273, https://doi. org/10.1016/j.matchemphys.2007.07.009.
- [5] S.R. Feldman, Principles of topical treatment: advancement in gel vehicle technology, J. Drugs Dermatol. 13 (4) (2014) 423–427.
- [6] M. Gou, X. Li, M. Dai, C. Gong, X. Wang, Y. Xie, H. Deng, L. Chen, X. Zhao, Z. Qian, Y. Wei, A novel injectable local hydrophobic drug delivery system: biodegradable nanoparticles in thermo-sensitive hydrogel, Int. J. Pharm. 359 (1) (2008) 228–233, https://doi.org/10.1016/j.ijpharm.2008.03.023.

- [7] D.J. Overstreet, D. Dutta, S.E. Stabenfeldt, B.L. Vernon, Injectable hydrogels, J. Polym. Sci. Part B 50 (13) (2012) 881–903, https://doi.org/10.1002/ polb.23081
- [8] M. Cully, Inflammatory diseases: hydrogel drug delivery for inflammatory bowel disease, Nat. Rev. Drug Discov. Lond. 14 (10) (2015) 678–679, https://doi.org/ 10.1038/nrd4744.
- [9] C. Lu, R.B. Yoganathan, M. Kociolek, C. Allen, Hydrogel containing silica shell cross-linked micelles for ocular drug delivery, J. Pharm. Sci. 102 (2) (2013) 627–637, https://doi.org/10.1002/jps.23390.
- [10] B. Amsden, Solute diffusion within hydrogels. Mechanisms and models, Macromolecules 31 (23) (1998) 8382–8395, https://doi.org/10.1021/ma980765f.
- [11] E. Axpe, D. Chan, G.S. Offeddu, Y. Chang, D. Merida, H.L. Hernandez, E.A. Appel, A multiscale model for solute diffusion in hydrogels, Macromolecules 52 (18) (2019) 6889–6897, https://doi.org/10.1021/acs.macromol.9b00753.
- [12] X. Huang, C.S. Brazel, On the importance and mechanisms of burst release in matrix-controlled drug delivery systems, J. Contr. Release 73 (2) (2001) 121–136, https://doi.org/10.1016/S0168-3659(01)00248-6.
- [13] C. Lu, A.S. Mikhail, X. Wang, M.A. Brook, C. Allen, Hydrogels containing core cross-linked block Co-polymer micelles, J. Biomater. Sci. Polym. Ed. 23 (8) (2012) 1069–1090, https://doi.org/10.1163/092050611X575414.
- [14] M. Jaiswal, M. Kumar, K. Pathak, Zero order delivery of itraconazole via polymeric micelles incorporated in situ ocular gel for the management of fungal keratitis, Colloids Surf. B Biointerfaces 130 (2015) 23–30, https://doi.org/10.1016/j. colsurfb.2015.03.059.
- [15] E. Ruel-Gariépy, G. Leclair, P. Hildgen, A. Gupta, J.-C. Leroux, Thermosensitive chitosan-based hydrogel containing liposomes for the delivery of hydrophilic molecules, J. Contr. Release 82 (2) (2002) 373–383, https://doi.org/10.1016/ S0168-3659(02)00146-3.
- [16] A. Suri, R. Campos, D.G. Rackus, N.J.S. Spiller, C. Richardson, L.-O. Pålsson, R. Kataky, Liposome-doped hydrogel for implantable tissue, Soft Matter 7 (15) (2011) 7071–7077, https://doi.org/10.1039/C1SM05530E.
- [17] J.W. Bae, D.H. Go, K.D. Park, S.J. Lee, Thermosensitive chitosan as an injectable carrier for local drug delivery, Macromol. Res. 14 (4) (2006) 461–465, https://doi. org/10.1007/BF03219111.
- [18] L.K. Widjaja, M. Bora, P.N.P.H. Chan, V. Lipik, T.T.L. Wong, S.S. Venkatraman, Hyaluronic acid-based nanocomposite hydrogels for ocular drug delivery applications, J. Biomed. Mater. Res. A 102 (9) (2014) 3056–3065, https://doi.org/ 10.1002/ibm.a.34976.
- [19] S. Grijalvo, J. Mayr, R. Eritja, D.D. Díaz, Biodegradable liposome-encapsulated hydrogels for biomedical applications: a marriage of convenience, Biomater. Sci. 4 (4) (2016) 555–574, https://doi.org/10.1039/C5BM00481K.
- [20] C. Creton, 50th anniversary perspective: networks and gels: soft but dynamic and tough, Macromolecules 50 (21) (2017) 8297–8316, https://doi.org/10.1021/acs. macromol.7b01698.
- [21] B. Jeong, Y.H. Bae, S.W. Kim, Drug release from biodegradable injectable thermosensitive hydrogel of PEG-PLGA-PEG triblock copolymers, J. Contr. Release 63 (1) (2000) 155–163, https://doi.org/10.1016/S0168-3659(99)00194-7
- [22] K.P. Mineart, Y. Lin, S.C. Desai, A.S. Krishnan, R.J. Spontak, M.D. Dickey, Ultrastretchable, cyclable and recyclable 1- and 2-dimensional conductors based on physically cross-linked thermoplastic elastomer gels, Soft Matter 9 (32) (2013) 7695–7700, https://doi.org/10.1039/c3sm51136g.
- [23] S. Srivastava, A.E. Levi, D.J. Goldfeld, M.V. Tirrell, Structure, morphology, and rheology of polyelectrolyte complex hydrogels formed by self-assembly of oppositely charged triblock polyelectrolytes, Macromolecules 53 (14) (2020) 5763–5774. https://doi.org/10.1021/acs.macromol.0c00847.
- 5763–5774, https://doi.org/10.1021/acs.macromol.0c00847.
 [24] D.A. Vega, J.M. Sebastian, Y.-L. Loo, R.A. Register, Phase behavior and viscoelastic properties of entangled block copolymer gels, J. Polym. Sci. Part B 39 (18) (2001) 2183–2197, https://doi.org/10.1002/polb.1192.
- [25] T.L. Chantawansri, A.J. Duncan, J. Ilavsky, K.K. Stokes, M.C. Berg, R.A. Mrozek, J. L. Lenhart, F.L. Beyer, J.W. Andzelm, Phase behavior of SEBS triblock copolymer gels, J. Polym. Sci. Part B 49 (20) (2011) 1479–1491, https://doi.org/10.1002/polb.22335.
- [26] T. Li, A.J. Senesi, B. Lee, Small angle X-ray scattering for nanoparticle Research, Chem. Rev. 116 (18) (2016) 11128–11180, https://doi.org/10.1021/acs. chemrev.5b00690.
- [27] K.P. Mineart, W.W. Walker, J. Mogollon-Santiana, B. Lee, A fourier transform infrared spectroscopy-based method for tracking diffusion in organogels, J. Polym. Sci. 58 (12) (2020) 1707–1716, https://doi.org/10.1002/pol.20200144.
- [28] C. Hansen, Hansen Solubility Parameters : A User's Handbook, second ed., CRC Press, Boca Raton, FL, USA, 2007.
- [29] E. Stefanis, C. Panayiotou, Prediction of hansen solubility parameters with a new group-contribution method, Int. J. Thermophys. 29 (2) (2008) 568–585, https://doi.org/10.1007/s10765-008-0415-z.
- [30] C.M. Hansen, A.L. Smith, Using hansen solubility parameters to correlate solubility of C60 fullerene in organic solvents and in polymers, Carbon 42 (8) (2004) 1591–1597, https://doi.org/10.1016/j.carbon.2004.02.011.
- [31] C.M. Hansen, Polymer additives and solubility parameters, Prog. Org. Coating 51 (2) (2004) 109–112, https://doi.org/10.1016/j.porgcoat.2004.05.003.
- [32] T.B. Nielsen, C.M. Hansen, Elastomer swelling and hansen solubility parameters, Polym. Test. 24 (8) (2005) 1054–1061, https://doi.org/10.1016/j. polymertesting 2005 05 007
- [33] J.H. Laurer, R. Bukovnik, R. Spontak, J. Morphological characteristics of SEBS thermoplastic elastomer gels, Macromolecules 29 (17) (1996) 5760–5762, https://doi.org/10.1021/ma9607271.

ARTICLE IN PRESS

K.P. Mineart et al. Polymer xxx (xxxx) xxx

- [34] J.H. Laurer, S.A. Khan, R.J. Spontak, M.M. Satkowski, J.T. Grothaus, S.D. Smith, J. S. Lin, Morphology and rheology of SIS and SEPS triblock copolymers in the presence of a midblock-selective solvent, Langmuir 15 (23) (1999) 7947–7955, https://doi.org/10.1021/la981441n.
- [35] S. Muto, Y. Aono, K. Meguro, Solubilization of TCNQ by anionic surfactants, Bull. Chem. Soc. Jpn. 46 (9) (1973) 2872–2873, https://doi.org/10.1246/bcsj.46.2872.
- [36] S. Muto, K. Meguro, The determination of the CMC of surfactants in some organic solvents, Bull. Chem. Soc. Jpn. 46 (5) (1973) 1316–1320, https://doi.org/ 10.1246/bcsi.46.1316.
- [37] G.N. Smith, P. Brown, S.E. Rogers, J. Eastoe, Evidence for a critical micelle concentration of surfactants in hydrocarbon solvents, Langmuir 29 (10) (2013) 3252–3258, https://doi.org/10.1021/la400117s.
- [38] M. Kotlarchyk, J.S. Huang, S.H. Chen, Structure of AOT reversed micelles determined by small-angle neutron scattering, J. Phys. Chem. 89 (20) (1985) 4382–4386, https://doi.org/10.1021/j100266a046.
- [39] D.J. Kinning, E.L. Thomas, Hard-sphere interactions between spherical domains in diblock copolymers, Macromolecules 17 (9) (1984) 1712–1718, https://doi.org/ 10.1021/ma00139a013.

- [40] G. Ungar, V. Tomašić, F. Xie, X. Zeng, Structure of liquid crystalline aerosol-OT and its alkylammonium salts, Langmuir 25 (18) (2009) 11067–11072, https://doi.org/ 10.1021/ja901385n
- [41] M. Tokita, Transport phenomena in gel, Gels 2 (2) (2016) 17, https://doi.org/ 10.3390/gels2020017.
- [42] M. Karvar, F. Strubbe, F. Beunis, R. Kemp, N. Smith, M. Goulding, K. Neyts, Investigation of various types of inverse micelles in nonpolar liquids using transient current measurements, Langmuir 30 (41) (2014) 12138–12143, https://doi.org/10.1021/la502287m.
- [43] P.G. Murphy, D.A. MacDonald, T.D. Lickly, Styrene migration from general-purpose and high-impact polystyrene into food-simulating solvents, Food Chem. Toxicol. 30 (3) (1992) 225–232, https://doi.org/10.1016/0278-6915(92)90037-L.
- [44] N. Ramesh, J.L. Duda, Predicting migration of trace amounts of styrene in poly (styrene) below the glass transition temperature, Food Chem. Toxicol. 39 (4) (2001) 355–360, https://doi.org/10.1016/S0278-6915(00)00146-0.
- [45] R. Shankar, A.S. Krishnan, T.K. Ghosh, R.J. Spontak, Triblock copolymer organogels as high-performance dielectric elastomers, Macromolecules 41 (16) (2008) 6100–6109, https://doi.org/10.1021/ma071903g.